GEOPHYSICS, VOL. 78, NO. 4 (JULY-AUGUST 2013); P. S221–S231, 15 FIGS., 2 TABLES.
10.1190/GEO2012-0211.1

Shot-profile true amplitude crosscorrelation imaging condition

B. Arntsen[1], A. Kritski[2], B. Ursin[1], and L. Amundsen[1]

ABSTRACT

The U/D imaging condition for shot profile migration can be used to estimate the angle dependent reflection coefficient, but is difficult to implement numerically because of the spectral division involved. Most techniques for stabilizing the division require a damping factor which might be difficult to estimate and which also introduces bias into the final result. A stable result can be achieved by approximating the imaging condition with a crosscorrelation of the up- and downgoing wavefields at zero time lag, but this will lead to incorrect amplitude-versus-angle (AVA) behavior of the estimated reflection coefficient. We use a simple model for wave propagation of primary reflections in the wavenumber frequency domain and invert the model with respect to the reflection coefficient. By using the properties of wavefield extrapolators it can then be shown that the reflection coefficients can be estimated by crosscorrelation of the upgoing wavefield and a downgoing wavefield where the initial wavefield is the inverse of the wavefield generated by a point source. The new imaging condition gives the correct AVA behavior for horizontal reflectors. For dipping reflectors it is shown that a postmigration correction factor can be used to recover the correct angle behavior of the reflection coefficient. The new imaging condition is numerically stable, does not involve damping factors, is simple to implement numerically, and is a simple modification of the classical crosscorrelation imaging condition. Numerical examples confirm the correct AVA behavior of the new imaging condition.

INTRODUCTION

Depth imaging should ideally be capable of recovering not only an image of the subsurface, but also angle-dependent reflection coefficients. For depth migration schemes based on high-frequency asymptotics, there are established and well-developed amplitude-preserving algorithms (Bleistein, 1987; Schleicher et al., 1993; Tygel et al., 1993; Ursin, 2004) capable of computing estimates of angle-dependent reflection coefficients in addition to structural images.

For migration based on one-way wave equations, Claerbout (1971) introduces an imaging condition for shot-profile migration using the ratio between up- and downgoing wavefields giving correct estimates of the reflection coefficient (Deng and McMechan, 2007). However, this condition is difficult to implement due to the instability of spectral division leading to increased noise level. A wide variety of approaches to stabilize Claerbout's (1971) imaging condition have been investigated by Cazzola et al. (2002), Valenciano and Biondi (2003), Zhang et al. (2005), Schleicher et al. (2008), and Ursin et al. (2012).

Claerbout (1971) also suggests an approximate crosscorrelation imaging condition for shot-profile migration which has been extensively used due to its simplicity and stability. Rickett and Sava (2002) extend this imaging condition to include offset information and to compute angle gathers. Designed for structural imaging, this approach does not give correct estimates of the amplitude-versus-angle (AVA) response.

We derive a modification of Claerbout's (1971) crosscorrelation imaging condition that produces common-angle gathers with correct AVA relationship. The method is simple to implement and requires only a modification of the initial wavefield in the downward propagation and decomposition into plane waves in the midpoint-slowness domain (de Bruin et al., 1990). The method estimates AVA responses from locally plane and dipping reflectors, given that the local dip angle is known.

Manuscript received by the Editor 12 June 2012; revised manuscript received 11 January 2013; published online 24 June 2013.
[1]Norwegian University of Science and Technology, Department of Petroleum Engineering and Applied Geophysics, Trondheim, Norway. E-mail: borge.arntsen@ntnu.no; bjorn.ursin@ntnu.no; lam@statoil.com.
[2]Statoil Research Centre, Trondheim, Norway. E-mail: akr@statoil.com.

In the next section, we consider a simple model for primary reflections and derive the new imaging condition by inverting the model with respect to the reflection coefficient. We also compare our method with other approaches to shot-profile migration. The section on numerical results demonstrate that correct AVA response can be obtained for simple models and a more realistic reservoir model.

IMAGING CONDITION

We consider a single shot record with a seismic source at lateral position $\mathbf{x}_s$ at the surface of an acoustic medium where the wave propagation velocity c and density ρ are functions of depth only. In the following we will only consider isotropic wave propagation, although the approach presented here can be generalized to the anisotropic case. We consider plane waves where the principal direction of propagation is taken along the x_3-axis ("depth") and the transverse axes are (x_1, x_2). The wavenumber is denoted by $\mathbf{m} = (k_1, k_2, k_3)$. We will also use the 2D horizontal wavenumber defined by $\mathbf{k} = (k_1, k_2)$. The wavenumber $\mathbf{m}$ is related to the slowness $\mathbf{p}$ by

$$\mathbf{m} = \omega \mathbf{p}, \tag{1}$$

where ω is the angular frequency and the vertical wavenumber k_3 is given by

$$k_3 = \begin{cases} \sqrt{(\omega/c)^2 - k_1^2 - k_2^2}, & \text{if } \sqrt{k_1^2 + k_2^2} \le \omega/c, \\ i\sqrt{k_1^2 + k_2^2 - (\omega/c)^2}, & \text{if } \sqrt{k_1^2 + k_2^2} > \omega/c. \end{cases} \tag{2}$$

Pressure-normalized imaging condition

The pressure and vertical component of the particle velocity can be decomposed into up- and downgoing waves. This decomposition is not unique (Ursin, 1983; Ursin et al., 2012), but the most common approach is to use so-called *pressure normalization*, where the upgoing wave U at depth x_3 can be related to the downgoing wavefield D at the same depth using a simplified model for primary reflections, as shown in equation A-18 in Appendix A,

$$U(\mathbf{k}, x_3, \omega) = R(\mathbf{k}, x_3) D(\mathbf{k}, x_3, \omega). \tag{3}$$

Here, R is the reflection coefficient, and the downgoing wavefield D at depth can be estimated from the downgoing wavefield at the surface D_0 by

$$D(\mathbf{k}, x_3, \omega) = \exp\left[\int_0^{x_3} ik_3(\zeta) \mathrm{d}\zeta\right] D_0(\mathbf{k}, \omega), \tag{4}$$

where D_0 is due to a point source (Ursin, 1983)

$$D_0(\mathbf{k}, \omega) = -\frac{2\pi S(\omega) \exp(-i\mathbf{q} \cdot \mathbf{x}_s)}{ik_3}. \tag{5}$$

Here, $S(\omega)$ is the source signature, $\mathbf{q} = (k_1, k_2)$ is the transverse wavenumber while $\mathbf{x}_s = (x_{s1}, x_{s2})$ is the source position. The upgoing wavefield is computed from the data U_0 at the surface

$$U(\mathbf{k}, x_3, \omega) = \exp\left[-\int_0^{x_3} ik_3(\zeta) \mathrm{d}\zeta\right] U_0(\mathbf{k}, \omega). \tag{6}$$

The reflection coefficient can be found from equation 3 as

$$R(\mathbf{k}, x_3) = \frac{U(\mathbf{k}, x_3, \omega)}{D(\mathbf{k}, x_3, \omega)}, \tag{7}$$

and by using equations 4 and 5, equation 7 becomes

$$R(\mathbf{k}, x_3, \omega) = U(\mathbf{k}, x_3, \omega) D'^*(\mathbf{k}, x_3, \omega), \tag{8}$$

where the new downgoing wavefield D'

$$D'(\mathbf{k}, x_3, \omega) = \left[\int_0^{x_3} ik_3(\zeta) \mathrm{d}\zeta\right] D_0'(\mathbf{k}, \omega) \tag{9}$$

is due to an initial inverse downgoing wavefield

$$D_0'(\mathbf{k}, \omega) = \exp(-i\mathbf{q} \cdot \mathbf{x}_s) \frac{ik_3 S(\omega)}{2\pi |S^2(\omega)|}. \tag{10}$$

The division by the source spectrum can be stabilized by adding a small number to the denominator.

The reflection coefficient in 8 can be Fourier-transformed over the wavenumbers and frequency to the spatial domain to obtain the convolution integral

$$R(\mathbf{x}, x_3, \omega) = \int \mathrm{d}\mathbf{x}' U(\mathbf{x} - \mathbf{x}', x_3, \omega) D'^*(\mathbf{x}', x_3, \omega), \tag{11}$$

where $\mathbf{x} = (x_1, x_2)$ and * represents the complex conjugate. The up- and downgoing wavefields only depend on the distance between the source position $\mathbf{x}_s$ and the arguments $\mathbf{x} - \mathbf{x}'$. The integration over $\mathbf{x}'$ can then be carried out over the source position $\mathbf{x}_s$ instead. We also introduce the subsurface midpoint- and offset coordinates $\mathbf{x}_m$ and $\mathbf{h}$ by the definitions $\mathbf{x} = 2\mathbf{x}_m - h$ and $\mathbf{x}' = \mathbf{x}_m - \mathbf{h}/2$. Finally averaging the reflection operator over frequency, one obtains after converting integrals to sums

$$R(\mathbf{x}_m, \mathbf{h}, x_3) = \frac{1}{(2\pi)} \sum_{\omega} \sum_{\mathbf{x}_s} U(\mathbf{x}_m + \mathbf{h}/2, x_3, \mathbf{x}_s) \times D'^*(\mathbf{x}_m - \mathbf{h}/2, x_3, \mathbf{x}_s), \tag{12}$$

where we have introduced the source coordinate $\mathbf{x}_s$ as an extra argument.

de Bruin et al. (1990) point out that the integration over frequency in equation 12 implies summation over plane waves with different angles. To ensure averaging the reflection operator over constant angles, de Bruin et al. (1990) introduce a mapping to slowness before summation. Following de Bruin et al. (1990), we then get the wave equation slowness transform

$$R_s(\mathbf{x}_m, \mathbf{p}_h, z, \mathbf{x}_s) = \frac{1}{(2\pi)} \sum_{\omega} \sum_{\mathbf{h}} \exp(i\omega \mathbf{p}_h \mathbf{h}) U(\omega, \mathbf{x}_m - \mathbf{h}/2, x_3, \mathbf{x}_s) D'^*(\omega, \mathbf{x}_m + \mathbf{h}/2, x_3, \mathbf{x}_s), \tag{13}$$

where the slowness $\mathbf{p}_h$ is related to the offset wavenumber $\mathbf{k}_h$ by $\mathbf{p}_h = \mathbf{k}_h/\omega$. Summation over source positions improves the estimate and ensures proper angular coverage,

$$R(\mathbf{x}_m, \mathbf{p}_h, x_3) = \sum_{\mathbf{x}_s} R_s(\mathbf{x}_m, \mathbf{p}_h, x_3, \mathbf{x}_s). \tag{14}$$

Equations 13 and 14 provide a new imaging condition that recovers correctly the angle-dependent plane-wave reflection coefficient given that the amplitudes of the up- and downgoing wavefields U and D are accurate. It avoids the division by the energy of the downgoing wavefield (Ursin et al., 2012) and gives a stable estimate of the plane-wave reflection coefficient.

Flux-normalized imaging condition

By using flux-normalized wavefields, the differential equations for the up- and downgoing waves become simpler and potentially will lead to more accurate wavefield extrapolation. The flux normalized wavefields $\tilde{U}$ and $\tilde{D}$ are related through the equation (see equation A-26 in Appendix A)

$$\tilde{U}(\mathbf{k}, x_3, \omega) = \tilde{R}(\mathbf{k}, x_3)\tilde{D}(\mathbf{k}, x_3, \omega), \tag{15}$$

where $\tilde{R}$ is given by equation A-25.

The upgoing wavefield $\tilde{U}_0$ at the surface is related to the pressure-normalized field U_0 by (Ursin et al., 2012)

$$\tilde{U}_0(\mathbf{k}, x_3, \omega) = \sqrt{\frac{2}{Z}} U_0(\mathbf{k}, \omega), \tag{16}$$

where the impedance Z is given by $Z = \rho\omega/k_3$. The initial inverse downgoing wavefield D' is obtained as (Ursin et al., 2012)

$$\tilde{D}_0'(\mathbf{k}, \omega) = -\frac{\sqrt{\frac{1}{2}k_3\rho_0\omega}}{2\pi S^*(\omega)}. \tag{17}$$

Using the new flux-normalized wavefields $\tilde{U}_0$ and $\tilde{D}_0'$, wave extrapolation can be performed as for the downgoing wavefield as in equations 4 and 6. The estimate of the plane-wave reflection coefficient is computed from

$$\tilde{R}(\mathbf{x}_m, \mathbf{p}_h, x_3) = \frac{1}{(2\pi)} \sum_{\omega} \sum_{\mathbf{x}_s} \sum_{\mathbf{h}} \exp(i\omega \mathbf{p}_h \mathbf{h}) \tilde{U}(\omega, \mathbf{x}_m - \mathbf{h}/2, x_3, \mathbf{x}_s) \tilde{D}'^*(\omega, \mathbf{x}_m + \mathbf{h}/2, x_3, \mathbf{x}_s). \tag{18}$$

Heterogeneous medium

The imaging conditions given above in equations 13 and 16 can be proved to be correct for heterogeneous media with smooth velocity variations. The up- and downgoing pressure-normalized wavefields can then be recursively extrapolated using the explicit operator approach (Holberg, 1988),

$$\begin{aligned} U(x_1, x_2, x_3 + \Delta x_3) &= \sum_{x_1', x_2'} f^*(x_1 - x_1', x_2 - x_2', \omega/c) \\ &\quad \times U(x_1', x_2', x_3), \\ D(x_1, x_2, x_3 + \Delta x_3) &= \sum_{x_1', x_2'} f(x_1 - x_1', x_2 - x_2', \omega/c) \\ &\quad \times D(x_1', x_2', x_3), \end{aligned} \tag{19}$$

where f is a band-limited approximation to the phase-shift operator depending on the ratio between the frequency and the local velocity, and Δx_3 is the discretization interval in the vertical direction. Equation 19 can also be used to extrapolate the flux-normalized wavefields $\tilde{U}$ and $\tilde{D}$.

RELATION TO OTHER IMAGING CONDITIONS

Rickett and Sava (2002) proposed the extended imaging condition given by

Table 1. Horizontally layered model, with density contrast between layers. The velocity is constant for all layers.

Layer thickness (m)	Velocity (m/s)	Density (kg/m^3)
1000	2000	1000
1000	2000	1200
1000	2000	1000
—	2000	1200

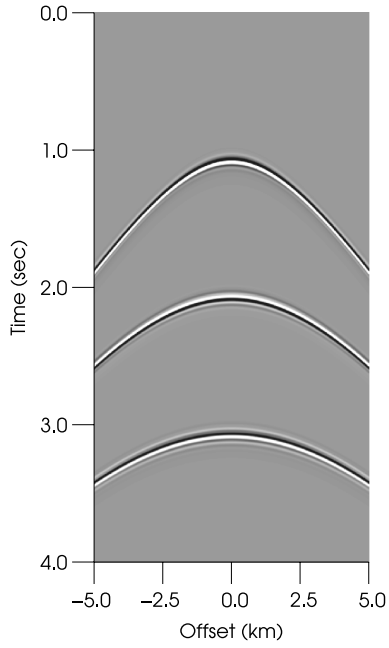

Figure 1. Shot record generated using the layered model given in Table 1.

$$R(\mathbf{x}_m, \mathbf{h}, x_3) = \frac{1}{2\pi} \sum_{\mathbf{x}_s} \sum_{\omega} U(\mathbf{x}_m - \mathbf{h}/2, x_3, \mathbf{x}_s) \times D^*(\mathbf{x}_m + \mathbf{h}/2, x_3, \mathbf{x}_s). \quad (20)$$

The imaging condition in equation 20 is similar to the imaging condition in equation 12, the only difference is that D' is substituted with D.

In the wavenumber-frequency domain, the estimate $\hat{R}$ of the reflection coefficient corresponding to the extended imaging condition (Rickett and Sava, 2002) is equal to

$$\hat{R}(x_3) = R(x_3) D_0 D_0{}^* = R(x_3) \frac{|S(\omega)|^2}{4\pi^2 k_3^2}. \quad (21)$$

Zhang and Sun (2008) propose an imaging condition where the initial downgoing wavefield is given by

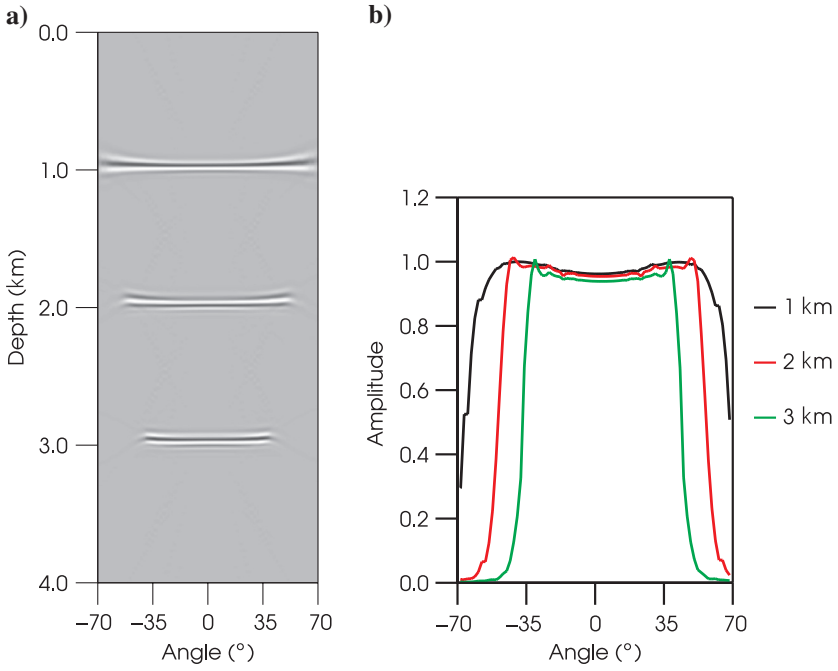

Figure 2. (a) Angle gather for the plane layered model given in Table 1 and (b) rms amplitude picks of the angle gathers. The AVA is seen to be constant, which is consistent with a model with density contrasts only.

Table 2. Horizontally layered model, with velocity contrast between layers. The density is constant for all layers.

Layer thickness (m)	Velocity (m/s)	Density (kg/m^3)
1000	2000	1000
1000	2200	1000
1000	2000	1000
—	2200	1000

$$\hat{D}_0(\mathbf{k}, \omega) = -\frac{\exp(-i\mathbf{q}_s \mathbf{x}_s) S(\omega)}{i\omega}, \quad (22)$$

which leads to the estimate of the reflection coefficient

$$\hat{R}(\mathbf{k}, x_3) = R(\mathbf{k}, x_3) \frac{|S(\omega)|^2}{2\pi k_3 \omega}. \quad (23)$$

Because k_3 is proportional to $(\omega/c)\cos(\phi)$, where ϕ is the reflection angle, it is seen that the imaging condition given by equation 21 gives an estimate of the reflection coefficient proportional to the inverse of $\cos^2(\phi)$, whereas the estimate obtained from equation 23 is proportional to the inverse of $\cos(\phi)$.

AVA GATHERS

In the preceding sections, we derived expressions for computing the reflection operator as a function of horizontal slowness $\mathbf{p}_h$. For a wave reflected from a plane dipping reflector and where the velocity can be assumed to be constant equal to c, the relation between the incidence angle ϕ and slowness $\mathbf{p}_h$ is given by (Rickett and Sava, 2002)

$$p_{hx} = \frac{1}{c} \sin(\phi) \cos(\alpha) \cos(\theta),$$
$$p_{hy} = \frac{1}{c} \sin(\phi) \cos(\alpha) \sin(\theta), \quad (24)$$

where ϕ is the reflection angle, α is the dip angle, and θ is the direction of the maximum down-dip direction. Equation 24 can be used to map the reflectivity from offset slowness to opening- and dip angle.

In Appendix B, it is shown that the reflection coefficient for a dipping plane reflector for the pressure-normalized case is given by

$$R(\phi, \alpha, x_3) = \left[\frac{2\cos(\phi - \alpha)}{\cos(\phi + \alpha) + \cos(\phi - \alpha)}\right] \times r(\phi - \alpha), \quad (25)$$

where r is the linearized plane-wave reflection coefficient. If we assume that the wave velocities in the neighborhood of a given midpoint location are approximately constant, we can use equation 25 to compute the plane-wave reflection coefficient from the reflection operator as

$$r(\phi - \alpha) = R(\phi, \alpha, x_3) \left[\frac{\cos(\phi - \alpha) + \cos(\phi + \alpha)}{2\cos(\phi - \alpha)}\right]. \quad (26)$$

For the flux-normalized approach, one gets

$$r(\phi - \alpha) = \tilde{R}(\phi, \alpha, x_3) \left[\frac{\cos(\phi - \alpha) + \cos(\phi + \alpha)}{2\sqrt{\cos(\phi + \alpha)\cos(\phi - \alpha)}}\right]. \quad (27)$$

If the background model used for the wave extrapolation is not accurate, the reflection coefficient will be mispositioned in depth.

If the dip angle α is incorrect, the estimated AVA response of the reflection coefficient will be affected.

The above relations show that, to successfully extract the plane-wave reflection coefficient from the reflection operator, the local reflector dip must be known. An advantage of equations 26 and 27 is that the computation of reflection coefficients can be performed postmigration.

In the next section, we demonstrate the use of the new imaging condition given by equation 14 using simple acoustic models and a more realistic elastic reservoir model.

NUMERICAL RESULTS

In the examples below, the reflection operator is computed using equations 13 and 14, while the plane-wave reflection coefficient is extracted using equation 26. The initial inverse wavefield D_0' is computed in the wavenumber frequency domain by equation 6.

Acoustic models

The model shown in Table 1 consists of four plane layers where the density is different in each layer, while the velocity is

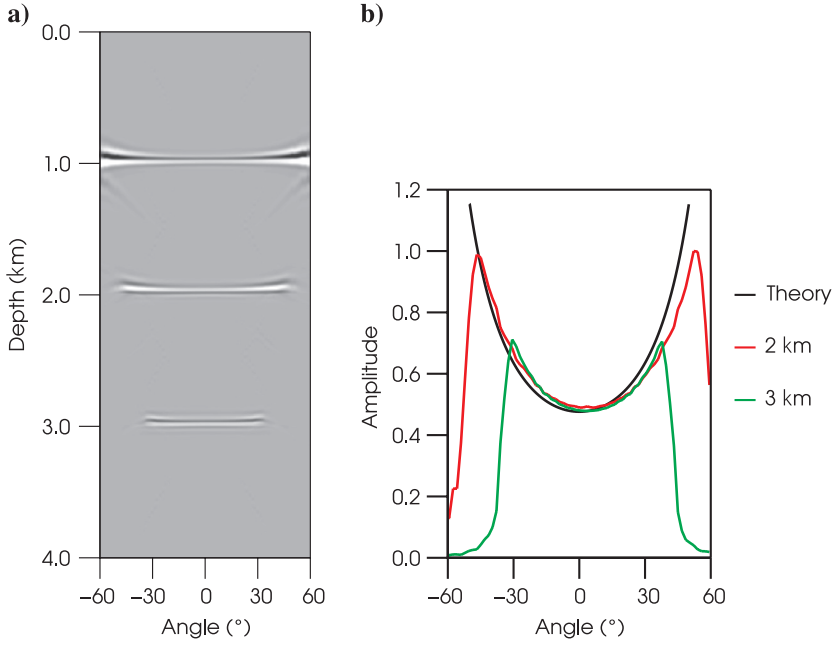

Figure 3. (a) Angle gather for the plane layered model given in Table 2 and (b) rms amplitude picks of the events at depths 2 and 3 km. The black solid line is the theoretical AVA response.

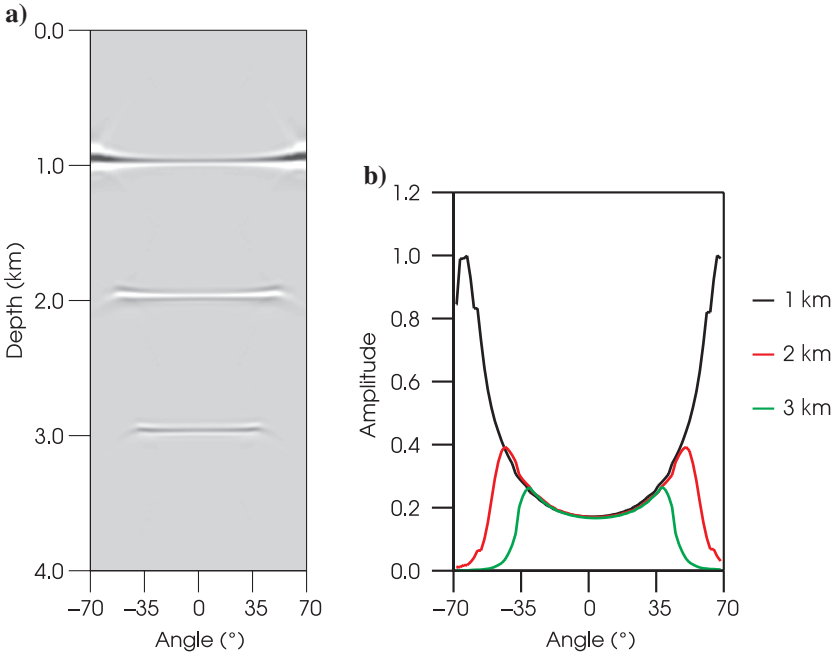

Figure 4. (a) Angle gather computed for the plane layered model given in Table 1 using Rickett and Sava (2002) extended imaging condition; (b) rms amplitude picks of the angle gather. The AVA is seen to give an incorrect AVA response, with strongly increasing amplitude with increasing angle.

kept constant throughout the model at 2000 m/s. Synthetic shot records were generated using the model given in Table 1 by a finite-difference acoustic modeling program. A split-spread acquisition geometry was used with 10 m receiver distance and a maximum half-offset of 5 km and a shot spacing of 10 m. The source signature was a Ricker wavelet with a peak frequency of 20 Hz. A single shot record is shown in Figure 1.

Equations 14 and 26 were used to compute the angle gather shown in Figure 2. Figure 2b shows rms amplitude picks extracted along the three events in the angle gather.

A common scale factor before plotting was applied to the three amplitude curves, such that the largest amplitude for the reflector at 1 km depth (black curve) is equal to one. The relative amplitudes between the reflectors are thus preserved. The AVA shows no significant angle dependence, which is expected in the case of reflectors with pure density contrast. Moreover, the amplitude levels of the three events are also approximately equal.

Table 2 contains a plane-layered model with velocity contrasts, and a corresponding shot record was computed as in the first example. An angle gather was computed in a similar way as for Figure 2 and shown in Figure 3 together with the rms amplitude picks for the events at a depth of 2 and 3 km. The black solid line shows the theoretical AVA response, which seems to fit well with the amplitudes picked from the angle gather.

In Figure 4, we have applied the extended imaging condition given by Rickett and Sava (2002) to the data for the model given in Table 1 where there is no AVA variation as shown in Figure 2. The AVA response in Figure 4 is seen to be incorrect, with amplitude increasing with angle. This is in accordance with equation 21 predicting amplitudes to increase by a factor $1/\cos^2(\phi)$, where ϕ is the reflection angle.

Figure 5 shows a velocity model with a layer dipping at approximately 18° and a flat reflector below. A synthetic split-spread survey with maximum offset of 5 km and a total of 1000 shots was acquired over this model. The first shotpoint was positioned at a horizontal distance of 5 km and the last at 15 km.

Figure 6a shows an angle gather computed at a horizontal position of 8 km in the model shown in Figure 5 using the shot records described above. Also, shown in Figure 6b are the rms amplitude picks of the two events in the angle gather. The event corresponding to the dipping reflector (black line) and the event corresponding to the flat reflector (red line) show the same AVA behavior, as expected.

The effect of ignoring the dip correction given by equation 26 is shown in Figure 7 where the angle gather has been computed using only equation 14, omitting the dip correction of equation 26. The red line shows the rms amplitude pick for the horizontal reflector while the black line shows the corresponding amplitude pick for the dipping reflector. As can be observed, the AVA response is incorrect if the dip correction is not applied.

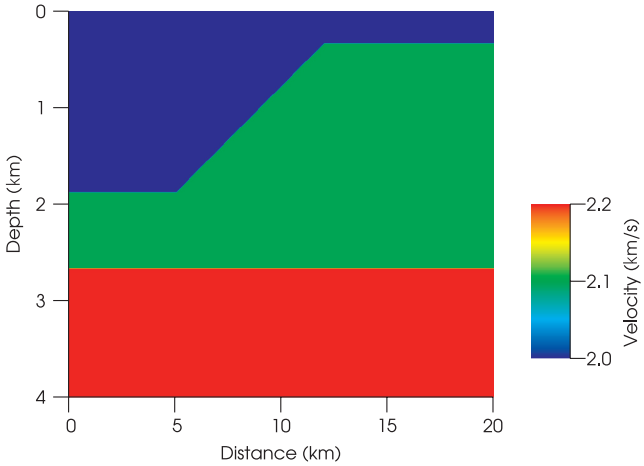

Figure 5. Velocity model with dipping layer.

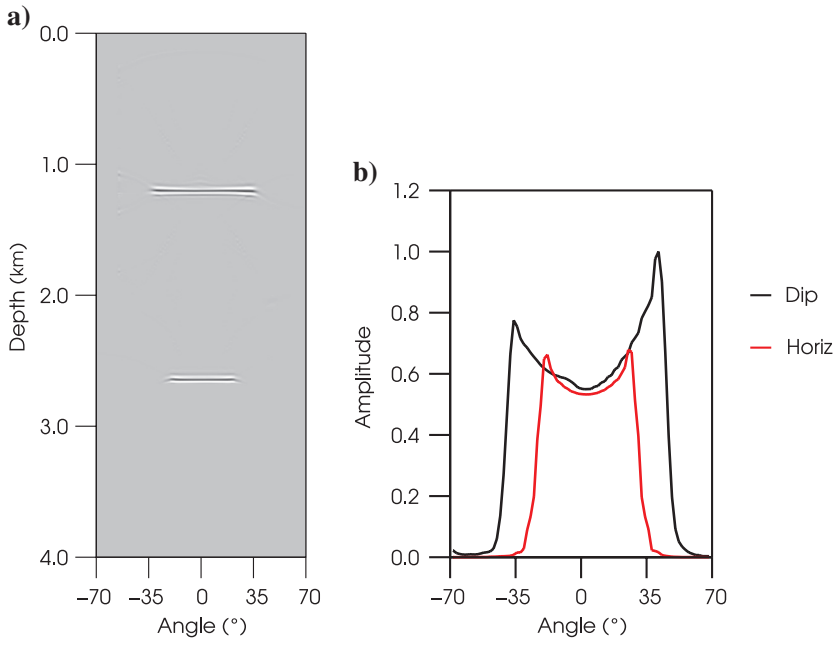

Figure 6. (a) Angle gather computed for the velocity model shown in Figure 5 and (b) rms amplitude picks for the dipping reflector (black line) and the plane reflector (red line).

Figure 8 shows sections obtained by stacking over all angles, with (left) and without (middle) the dip correction.

The difference (right) between these two sections is significant, but not large. The angular coverage increases in the up-dip direction due to the acquisition geometry, causing the difference to be larger for the upper part of the reflector. In Figure 9, only a narrow angle range from 23° to 25° have been stacked. The illumination of the dipping reflector is more even in this angle range, the difference is still significant, but not large.

Elastic reservoir model

The imaging condition developed in the preceding sections is valid for an acoustic medium, with acoustic reflection coefficients. In a real data case, the reflection coefficients are elastic. However, the model for primary reflections given in equation 1 is approximately valid, given that the acoustic reflection operator R is replaced with the corresponding elastic reflection operator R_{pp} (Aki and Richards, 1980). This implies that we neglect amplitude loss due to conversions from P-waves to S-waves.

Figure 10 shows a velocity model of the North Sea. An oil reservoir is located in the middle tilted fault block at a depth of approximately 2 km. An elastic finite-difference program was used to compute a synthetic marine survey across the velocity model. Angle gathers were computed using the new imaging condition as described in the previous sections, and angle stacks with angles ranging from 8° to 15° and 25° to 40° are shown in Figures 11 and 12, respectively.

Figure 13 shows an angle gather computed at a horizontal position of 1.7 km, while Figure 14 shows amplitude picks from the gather at the top reservoir reflector located at a depth of 1.850 km and the oil-water contact at a depth of 1.940 km. Comparison with the reflection coefficients computed from the P-wave, S-wave, and density models shows that the new imaging condition

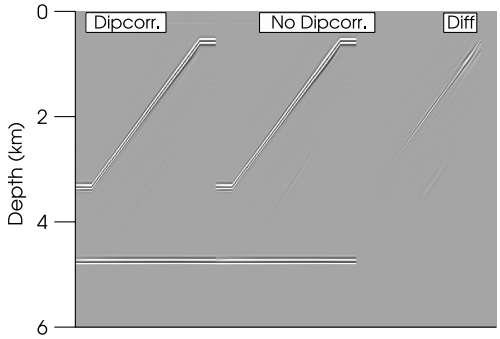

Figure 8. Stack sections using the data obtained from the model shown in Figure 5. All angles were included in the stacks. The left-hand section was produced from dip corrected angle gathers, while the section in the middle was produced from angle gathers with no dip correction. The section to the right shows the difference.

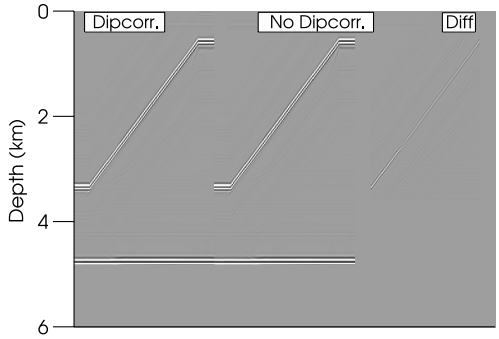

Figure 9. Stack sections using the data obtained from the model shown in Figure 5. Angles between 23° and 25° were included in the stacks. The left-hand section were produced from dip-corrected angle gathers, while the section in the middle was produced from angle gathers with no dip correction. The section to the right shows the difference.

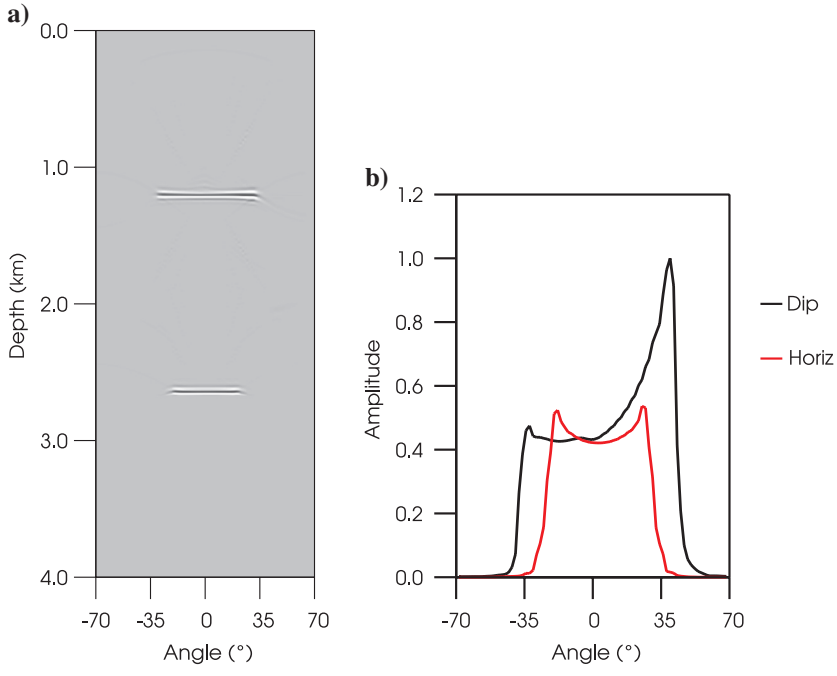

Figure 7. (a) Angle gather computed for the velocity model shown in Figure 5 . No dip correction was applied to the gather. (b) rms amplitude picks for the dipping reflector (black line) and the plane reflector (red line).

reproduces the true AVA response, except for small angles, where the estimates are incorrect.

The dip correction given by equation 26 is insignificant for the range of dips for most of the reflectors shown in Figure 14, but will make a difference for the reflections from the steep fault planes, as shown in Figure 15. The AVA response is significantly different when the dip correction is applied (circles) and when ignored (crosses).

DISCUSSION

To be able to extract reliable AVA responses from seismic data, there are several issues involved, two of them being the accuracy of the wavefield extrapolation and the imaging condition itself. Here, we deal with the imaging condition and assume that the up- and downgoing wavefields can be computed with sufficient accuracy.

The simple dip correction given by equation 26 is only valid for small contrasts in impedance and for small dip angles. Separate

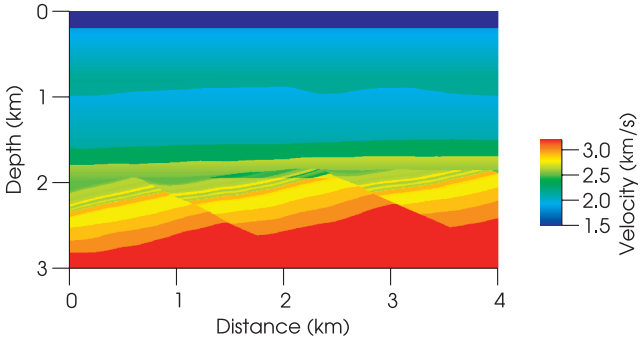

Figure 10. P-wave velocity for the elastic reservoir model.

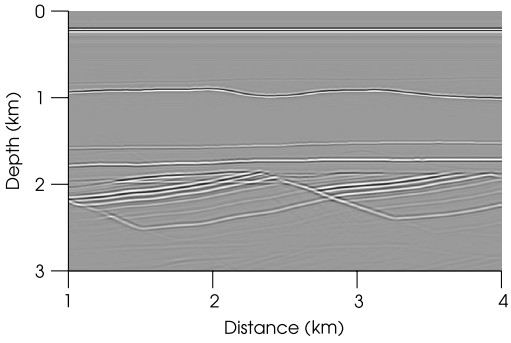

Figure 11. Stack of angle gathers between 8° and 15° of the elastic reservoir model.

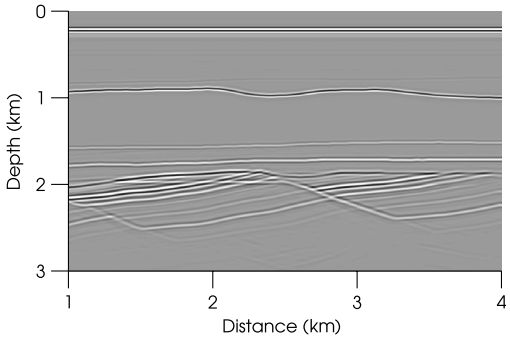

Figure 12. Stack of angle gathers between 24° and 40° of the elastic reservoir model.

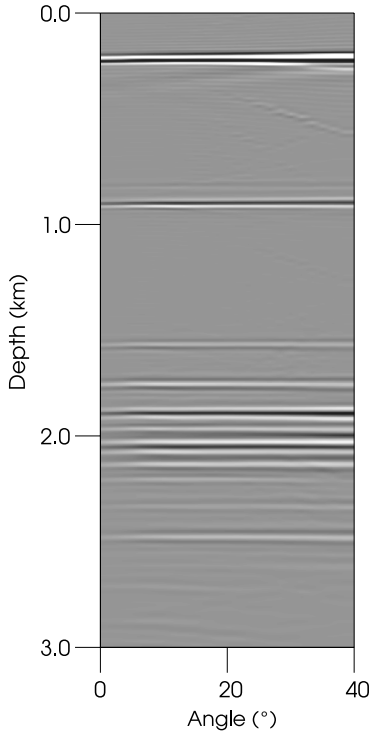

Figure 13. Angle gather at horizontal position of 1700 m.

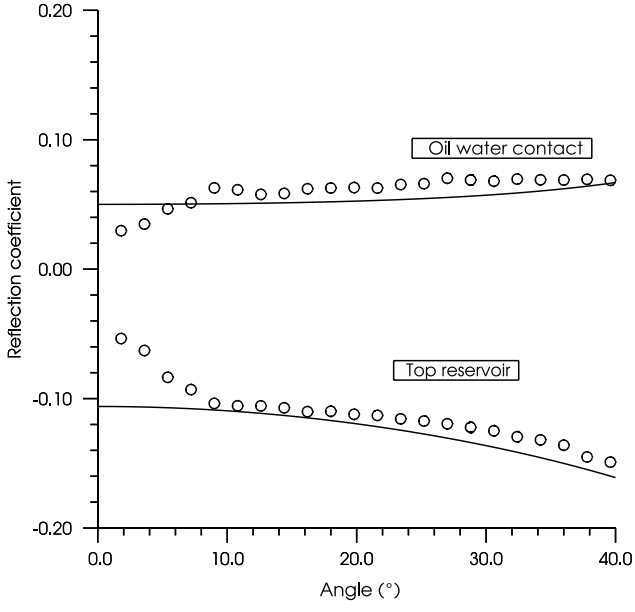

Figure 14. Amplitude picks using the angle gather in Figure 13 showing the oil-water contact (above) and top-reservoir (bottom). Circles shows the picks, while the solid line shows exact elastic reflection coefficients.

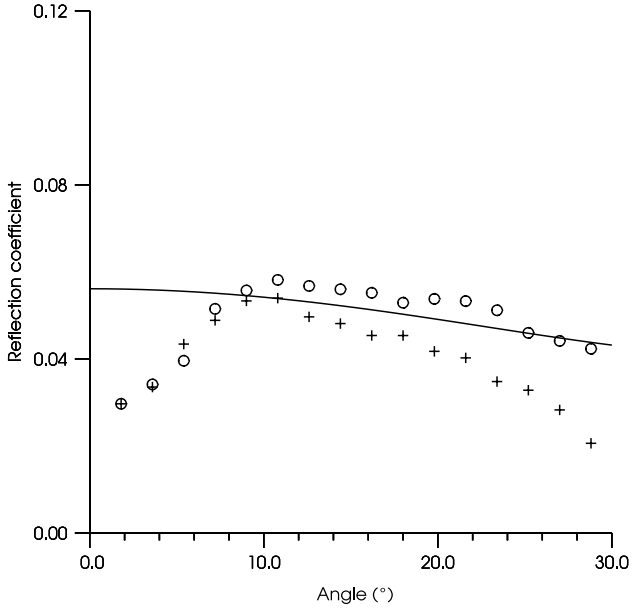

Figure 15. Amplitudes (circles) picked from an angle gather positioned at a distance of 2 km for a reflector at a depth of 2.2 km. The dip of the reflector is 36°. The crosses shows the corresponding picks without applying the dip correction given by 26.

information of the local dip is required as well, and can not be provided by the algorithm itself.

The actual acquisition parameters are a limiting factor for the accuracy of the AVA response; Figures 14 and 15 demonstrate that a marine single-spread geometry will lead to incorrect estimates of the reflection coefficients for small angles. This can be somewhat improved by careful tapering of the input data but cannot be completely removed unless a better split-spread type geometry is used (as in ocean-bottom cable surveys).

The approach presented here for true-amplitude migration is valid also for the 3D case provided that the crossline sampling interval is small enough to sample the wavefield properly. This is not usually the case for conventional streamer geometries because streamer separation is typically of the order of 100 m, and in favorable cases as small as 50 m. This is probably not enough to estimate the correct crossline AVA response, but might be adequate to compensate for the spherical spreading to ensure correct prediction of the inline AVA response.

CONCLUSIONS

We propose a new source initial condition which stabilizes the classical imaging condition. The new modified imaging condition is of crosscorrelation type and avoids instabilities associated with division of wavefields. This results in a crosscorrelation wave-equation angle transform which is a direct estimate of the plane-wave reflection coefficient for a plane horizontal reflector. For a dipping plane, we propose a simple dip and azimuth correction which gives an approximate estimate of the plane-wave reflection coefficient.

The crosscorrelation imaging condition proposed by Claerbout (1971), and extended by Rickett and Sava (2002), can be easily modified to produce correct AVA gathers for locally plane and dipping reflectors. This only involves changing the initial point-source wavefield to a modified wavefield with a radiation pattern different from a point source and a postmigration dip-correction.

The results were derived for a scalar wave equation, but numerical results show that they can approximately be extended to PP reflections in elastic media.

ACKNOWLEDGMENTS

We thank the Norwegian Research Council, the sponsors of the ROSE project and Statoil for financial support. Bjørn Ursin has received financial support from VISTA. We also thank John Etgen and three anonymous reviewers for constructive comments which helped to improve the paper.

APPENDIX A

ONE-WAY WAVE EQUATIONS

We consider an acoustic medium where the density $\rho(z)$ and velocity $c(z)$ is a function of depth only. After Fourier transforming the equations of motion over frequency ω and horizontal wavenumbers $\mathbf{k} = k_1, k_2$, one obtains the following matrix equation for the pressure P and the vertical particle velocity V_3 (Ursin, 1983):

$$\partial_3 \mathbf{b} = i\omega A \mathbf{b}, \tag{A-1}$$

where the matrix $\mathbf{A}$ is

$$\mathbf{A} = \begin{bmatrix} 0 & -\rho \\ \frac{1}{\rho}\left(\frac{1}{c^2} - \frac{k_1^2+k_2^2}{\omega^2}\right) & 0 \end{bmatrix} \tag{A-2}$$

and the vector $\mathbf{b}$ is

$$\mathbf{b} = \begin{bmatrix} P \\ V_3 \end{bmatrix}. \tag{A-3}$$

The up- and downgoing waves U and D are related to the pressure and vertical particle velocity through the linear transformation

$$\mathbf{w} = \begin{bmatrix} U \\ D \end{bmatrix} = \mathbf{L}^{-1}\mathbf{b}. \tag{A-4}$$

Substituting $\mathbf{w}$ for $\mathbf{b}$ in equation A-1 leads to the differential equation for $\mathbf{w}$

$$\partial_3 \mathbf{w} = (i\omega\mathbf{\Lambda} - \mathbf{L}^{-1}\partial_3\mathbf{L})\mathbf{w}, \tag{A-5}$$

where $\mathbf{\Lambda}$ is a diagonal matrix composed of the eigenvalues p_3^u and p_3^d of $\mathbf{A}$

$$\mathbf{\Lambda} = \mathbf{L}^{-1}\mathbf{A}\mathbf{L} = \begin{bmatrix} -p_3^u & 0 \\ 0 & p_3^d \end{bmatrix}. \tag{A-6}$$

We will also make use of the impedances $Z^d = \rho/p_3^d$ and $Z^u = \rho/p_3^u$.

Pressure-normalized wavefields

The eigenvalue matrix of $\mathbf{A}$ can be scaled in different ways. The so-called *pressure-normalized scaling* corresponds to the following eigenvalue matrix:

$$\mathbf{L} = \begin{bmatrix} 1 & 1 \\ -1/Z^u & 1/Z^d \end{bmatrix}, \tag{A-7}$$

with inverse

$$\mathbf{L}^{-1} = \frac{1}{Z^u + Z^d} \begin{bmatrix} Z^u & -Z^d Z^u \\ Z^d & -Z^d Z^u \end{bmatrix}. \tag{A-8}$$

The differential equation A-5 becomes

$$\partial_3 \mathbf{w} = i\omega \begin{bmatrix} -p_3^u & 0 \\ 0 & p_3^d \end{bmatrix} \mathbf{w} + \frac{2}{Z^u + Z^d} \times \begin{bmatrix} -Z^d r(Z^u) & Z^u r(Z^d) \\ -Z^d r(Z^u) & Z^u r(Z^d) \end{bmatrix} \mathbf{w}, \tag{A-9}$$

where $r(Z)$ is given by

$$r(Z) = \frac{1}{2} Z^{-1} \partial_3 Z. \tag{A-10}$$

Neglecting the interaction between up- and downgoing waves leads to the following simplified differential equation for $\mathbf{w}$:

$$\partial_3 \mathbf{w} = i\omega \begin{bmatrix} -p_3^u & 0 \\ 0 & p_3^d \end{bmatrix} \mathbf{w}, \tag{A-11}$$

with solutions

$$U(x_3) = \exp\left(- \int_0^{x_3} i k_3^u(\zeta) d\zeta \right) U_0 \tag{A-12}$$

and

$$D(x_3) = \exp\left(\int_0^{x_3} i k_3^d(\zeta) d\zeta \right) D_0. \tag{A-13}$$

Here, D_0 is the initial downgoing wavefield at the surface for a point source, and U_0 is the measured data at the surface. This solution completely ignores the interaction between the up- and downgoing waves, but a slightly better solution taking the interaction partly into account can be obtained by inserting the approximate solution for the downgoing wavefield given by equation A-13 back into the right-hand side of equation A-9. By neglecting the diagonal terms and solving for U, one gets

$$U(x_3) = \exp\left[- \int_0^{x_3} i k_3^u(\zeta) \mathrm{d}\zeta \right] \int_0^{x_3} \exp\left[\int_0^{\zeta} i k_3^d(\zeta') \mathrm{d}\zeta' \right] \times R(\zeta) D(\zeta) d\zeta, \tag{A-14}$$

where R is given by

$$R(x_3) = \frac{2Z^u(x_3)}{Z^u(x_3) + Z^d(x_3)} r[Z^d(x_3)]. \tag{A-15}$$

In the simplified case where the reflections are caused by abrupt changes in the material parameters, R can be described by

$$R = R(x_3')\delta(x_3' - x_3), \tag{A-16}$$

and the upgoing wave U is then related to the downgoing wave D by

$$U(x_3) = R(x_3) \exp[i(k_3^d - k_3^u)x_3] D(x_3). \tag{A-17}$$

For a horizontal interface, $k_3^u = k_3^d$ and we get

$$U(x_3) = R(x_3) D(x_3). \tag{A-18}$$

Flux-normalized wavefields

By scaling the eigenvalue matrix of $\mathbf{A}$ in the following way

$$\tilde{\mathbf{L}} = \frac{1}{\sqrt{2}} \begin{bmatrix} \sqrt{Z^u} & \sqrt{Z^d} \\ -1/\sqrt{Z^u} & 1/\sqrt{Z^d} \end{bmatrix}, \tag{A-19}$$

we get the so-called *flux-normalization*. The inverse of $\tilde{\mathbf{L}}$ is

$$\tilde{\mathbf{L}}^{-1} = \frac{1}{\sqrt{2}(Z^u + Z^d)} \begin{bmatrix} \sqrt{Z^u} & -Z^d\sqrt{Z^u} \\ \sqrt{Z^d} & Z^u\sqrt{Z^d} \end{bmatrix}. \tag{A-20}$$

The differential equation A-5 becomes

$$\partial_3 \mathbf{w} = i\omega \begin{bmatrix} -p_3^u & 0 \\ 0 & p_3^d \end{bmatrix} \mathbf{w} + \frac{1}{Z^u + Z^d} \times \begin{bmatrix} (Z^u - Z^d) r(Z^u) & \sqrt{Z^u Z^d} r(Z^d) \\ \sqrt{Z^u Z^d} r(Z^u) & (Z^u - Z^d) r(Z^d) \end{bmatrix} \mathbf{w}. \tag{A-21}$$

Neglecting the last term in equation A-21 leads to

$$\tilde{U}(x_3) = \exp\left(- \int_0^{x_3} i k_3^u(\zeta) d\zeta \right) \tilde{U}_0 \tag{A-22}$$

and

$$\tilde{D}(x_3) = \exp\left(\int_0^{x_3} i k_3^d(\zeta) \mathrm{d}\zeta \right) \tilde{D}_0. \tag{A-23}$$

Inserting equation A-23 into the right-hand side of equation A-21 and neglecting the diagonal terms gives an expression for the upgoing wavefield

$$\tilde{U}(x_3) = \exp\left[- \int_0^{x_3} i k_3^u(\zeta) \mathrm{d}\zeta \right] \int_0^{x_3} \exp\left[\int_0^{\zeta} i k_3^d(\zeta') d\zeta' \right] \times \tilde{R}(\zeta) D(\zeta) \mathrm{d}\zeta, \tag{A-24}$$

where $\tilde{R}$ is given by

$$\tilde{R}(x_3) = \frac{2\sqrt{Z^u(x_3)Z^d(x_3)}}{Z^u(x_3) + Z^d(x_3)} r[Z^d(x_3)]. \quad \text{(A-25)}$$

In the simplified case where the reflections are caused by abrupt changes in the material parameters, the upgoing wave $\tilde{U}$ is then related to the downgoing wave $\tilde{D}$ by

$$\tilde{U}(x_3) = \tilde{R}(x_3) \exp[i(k_3^d - k_3^u)x_3]\tilde{D}(x_3). \quad \text{(A-26)}$$

For a plane-horizontal interface, $k_3^u = k_3^d$ and we then get

$$\tilde{U}(x_3) = \tilde{R}(x_3)\tilde{D}(x_3). \quad \text{(A-27)}$$

APPENDIX B

AMPLITUDE CORRECTION FOR DIPPING LAYER

We consider an interface with dip angle α relative to the vertical direction and azimuth angle θ in the direction of maximum dip. A downgoing wave reflected at the interface has an incoming angle equal to ϕ, measured relative to the surface normal of the interface. Under an isotropic assumption, due to Snell's law, the outgoing angle is also equal to ϕ. By simple geometry, the incoming and outgoing angles θ_u and θ_d measured relative to the vertical direction is given by

$$\theta_u = \phi + \alpha, \quad \theta_d = \phi - \alpha. \quad \text{(B-1)}$$

The vertical slowness p_3 is given by

$$p_3^d = \cos(\phi - \alpha)/c, \quad p_3^u = \cos(\phi + \alpha)/c, \quad \text{(B-2)}$$

which gives the impedances Z^d and Z^u

$$Z^d = \rho c/\cos(\phi - \alpha) \quad Z^u = \rho c/\cos(\phi + \alpha). \quad \text{(B-3)}$$

From equation A-15, we have for the reflection coefficient for pressure-normalized waves

$$R(x_3) = \frac{2\cos(\phi + \alpha)}{\cos(\phi - \alpha) + \cos(\phi + \alpha)} r(x_3), \quad \text{(B-4)}$$

and for the flux-normalized case we have, similarly, from equation A-25

$$\tilde{R}(x_3) = \frac{2\sqrt{\cos(\phi + \alpha)\cos(\phi - \alpha)}}{\cos(\phi - \alpha) + \cos(\phi + \alpha)} r(x_3). \quad \text{(B-5)}$$

From equations B-4 and B-5, it is clear that the plane-wave reflection coefficient for a plane layer can easily be obtained from equations B-4 and B-5.

REFERENCES

Aki, K., and P. G. Richards, 1980, Quantitative seismology: W.H. Freeman and Co.

Bleistein, N., 1987, On the imaging of reflectors in the earth: Geophysics, **52**, 931–942, doi: 10.1190/1.1442363.

Cazzola, L., M. Arienti, E. Bonomi, and G. Cardone, 2002, Amplitude-preserving Monte Carlo 3D prestack migration: 64th Conference and Exhibition, EAGE, Extended Abstracts, B009.

Claerbout, J. F., 1971, Toward a unified theory of reflector mapping: Geophysics, **36**, 467–481, doi: 10.1190/1.1440185.

de Bruin, C., C. Wapenaar, and A. Berkhout, 1990, Angle-dependent reflectivity by means of prestack migration: Geophysics, **55**, 1223–1234, doi: 10.1190/1.1442938.

Deng, F., and G. A. McMechan, 2007, True-amplitude prestack depth migration: Geophysics, **72**, no. 3, S155–S166, doi: 10.1190/1.2714334.

Holberg, O., 1988, Towards optimum one-way wave propagation: Geophysical Prospecting, **36**, 99–114, doi: 10.1111/j.1365-2478.1988.tb02154.x.

Rickett, J., and P. C. Sava, 2002, Offset and angle-domain common image-point gathers for shot-profile migration: Geophysics, **67**, 883–889, doi: 10.1190/1.1484531.

Schleicher, J., J. C. Costa, and A. Novais, 2008, A comparison of imaging conditions for wave-equation shot-profile migration: Geophysics, **73**, no. 6, S219–S227, doi: 10.1190/1.2976776.

Schleicher, J., M. Tygel, and P. Hubral, 1993, 3-D true-amplitude finite-offset migration: Geophysics, **58**, 1112–1126, doi: 10.1190/1.1443495.

Tygel, M., J. Schleicher, P. Hubral, and C. Hanitzsch, 1993, Multiple weights in diffraction stack migration: 63rd Annual International Meeting, SEG, Expanded Abstracts, 1040–1043.

Ursin, B., 1983, Review of elastic and electromagnetic wave propagation in layered media: Geophysics, **48**, 1063–1081, doi: 10.1190/1.1441529.

Ursin, B., 2004, Parameter inversion and angle migration in anisotropic elastic media: Geophysics, **69**, 1125–1142, doi: 10.1190/1.1801931.

Ursin, B., O. Pedersen, and B. Arntsen, 2012, Flux normalized wavefield decomposition and migration of seismic data: Geophysics, **77**, no. 3, S83–S92, doi: 10.1190/geo2011-0234.1.

Valenciano, A. A., and B. Biondi, 2003, 2D deconvolution imaging condition for shot-profile migration: 73rd Annual International Meeting, SEG, Expanded Abstracts, 1059–1062.

Zhang, Y., and J. Sun, 2008, Practical issues of reverse time migration: True-amplitude gathers, noise removal and harmonic-source encoding: 70th Conference and Exhibition, EAGE, Extended Abstracts, F047.

Zhang, Y., G. Zhang, and N. Bleistein, 2005, Theory of true-amplitude one-way wave equations and true-amplitude common-shot migration: Geophysics, **70**, no. 4, E1–E10, doi: 10.1190/1.1988182.